

Exact diagonalization study of the anisotropic Heisenberg model related to YbMgGaO₄

Muwei Wu, Dao-Xin Yao,^{*} and Han-Qing Wu[†]

State Key Laboratory of Optoelectronic Materials and Technologies,
School of Physics, Sun Yat-sen University, Guangzhou, 510275, China
(Dated: April 20, 2022)

Employing exact diagonalization, we systematically study the anisotropic Heisenberg model which is related to rare-earth triangular-lattice materials. From the finite-size low-energy spectra and the finite-size scalings of magnetic orders, we probe the full 3D phase diagram and identify all the phases. There is a large region of quantum spin liquid (QSL) phase in the model with nearest-neighbor anisotropic exchange interactions. However, the QSL region is different from previous study by density matrix renormalization group. After adding the next-nearest-neighbor interaction, this phase can adiabatically connect to quantum spin liquid phase in the $J_1 - J_2$ triangular Heisenberg model. More importantly, We explore the magnetization curves of different phases and reproduce the 1/3-magnetization plateau in the quantum spin liquid phase region. And, to study the possible chemical disorders in real materials, we consider the randomness of exchange interactions and find no spin glass order even in the strongest bond randomness case. Our comprehensive ED study can give detailed insightful understandings of the microscopic Hamiltonian related to the YbMgGaO₄ and some other related rare-earth triangular-lattice materials.

PACS numbers: 71.27.+a, 02.70.-c, 73.43.Nq, 75.10.Jm, 75.10.Kt, 75.10.Nr

Introduction Quantum spin liquid (QSL) phase [1] is an exotic quantum phase of matter beyond the Landau-Ginzburg-Wilson symmetry-breaking paradigm and displays rich physics, like nonlocal fractional excitations, long-range entanglement and emergent gauge field. QSLs are more likely to be found in frustrated spin systems, such as triangular and Kagome lattices. The geometric frustration and quantum fluctuation may prevent any magnetic long-range ordering even at zero temperature.

In recent years, two-dimensional rare-earth-based frustrated magnets play an important role and gain much efforts to realize the QSLs. Among that, YbMgGaO₄ [2–8] and rare-earth chalcogenide family NaYbCh₂ (Ch = O, S, Se) [9], are perfect triangular layer compounds with no structural or magnetic transition down to very low temperature. Especially, the broad continuum of magnetic excitation in the inelastic neutron scattering reveals a possible $U(1)$ QSL with a spinon Fermi surface [6, 10, 11]. Unprecedentedly, the magnetic excitation in the fully polarized state at sufficient high field remains very broad in both energy and wave vector, indicating the possible of disorders caused by the site-mixing of Mg/Ga, giving rising to the distributions of the effective spin-1/2 g factors and the magnetic couplings [5]. In fact, one recent experiment has observed some spin-glass-like behaviors both in the YbMgGaO₄ and its sister compound YbZnGaO₄ [12]. But another experiment seems exclude a true spin freezing in YbMgGaO₄ [8].

To understand macroscopic behaviors of these materials, an easy-plane XXZ Hamiltonian with anisotropic exchange interactions was proposed to describe the effective spin-1/2 interactions [3]. This microscopic Hamiltonian was studied by the Luttinger-Tisza method, the classical Monte Carlo simulation, the self-consistent spin wave

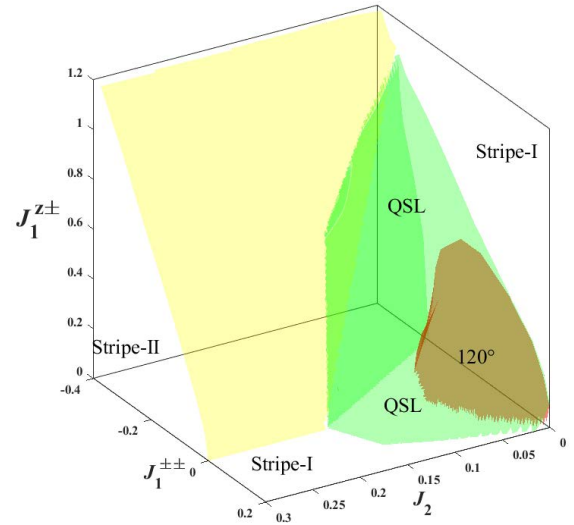


FIG. 1. The 3D phase diagram of anisotropic triangular Heisenberg model related to YbMgGaO₄ in the $J_2 - J_1^{\pm\pm} - J_1^{z\pm}$ parameter space. Four distinct phases, including 120° Néel phase, two stripe phases and a quantum spin liquid phase, are reproduced by our ED calculations.

theory, exact diagonalization (ED), density-matrix renormalization group (DMRG) and variational Monte Carlo (VMC) [13–23]. In this paper, we use ED to study this anisotropic Heisenberg model afresh. We depict the comprehensive 3D phase boundaries using extensive finite-size scaling. We have also studied the magnetic field effects and the bond randomness effects. Many details about the phases have been revealed and will provide further insightful understanding of the YbMgGaO₄ and other related materials.

Model and method The generic spin Hamiltonian of YbMgGaO_4 under $R\bar{3}m$ space symmetry group on the triangular lattice reads,

$$H = \sum_{\langle i,j \rangle} [J_1 S_i^z S_j^z + \frac{\alpha J_1}{2} (S_i^+ S_j^- + S_i^- S_j^+)] \\ + J_1^{\pm\pm} (\gamma_{ij} S_i^+ S_j^+ + \gamma_{ij}^* S_i^- S_j^-) \\ - \frac{i J_1^{\pm\pm}}{2} (\gamma_{ij}^* S_i^+ S_j^z - \gamma_{ij} S_i^- S_j^z + \langle i \leftrightarrow j \rangle) \\ + \sum_{\langle\langle i,j \rangle\rangle} [J_2 S_i^z S_j^z + \frac{\alpha J_2}{2} (S_i^+ S_j^- + S_i^- S_j^+)] \\ + \mu_0 \mu_B \sum_i [g_{\perp} (h_x S_i^x + h_y S_i^y) + g_{\parallel} h_z S_i^z]$$

Where $J_1^{\pm\pm}$ and $J_1^{z\pm}$ arise from the strong spin-orbital coupling, $\gamma_{ij} = 1, e^{-i2\pi/3}, e^{i2\pi/3}$ is for the bond along three principle axes, respectively. In the following calculations, we set the XXZ anisotropic $\alpha = 1.317$ [24] and set $J_1 = 1$ for energy unit. In the bond randomness case, The interaction strengths J_{ij} are uniformly distributed in the range $[J_{ij}(1 - \Delta), J_{ij}(1 + \Delta)]$

which are controlled by Δ . $\Delta = 1$ corresponds to the strongest bond randomness case. In the following, we define $H_{\perp} = \mu_0 \mu_B g_{\perp} \sqrt{h_x^2 + h_y^2}$, $H_{\parallel} = \mu_0 \mu_B g_{\parallel} h_z$ as the magnetic-field strengths to simplify the notations.

To get the phase boundaries, we have defined two kinds of magnetic order parameters. The first is the square sublattice magnetization for the 120° Néel phase [23, 25, 26]: $m_N^2 = \frac{1}{3} \sum_{\alpha=1}^3 \left[\frac{1}{(N/6)(N/6+1)} \left\langle \left(\sum_{i \in \alpha} \mathbf{S}_i \right)^2 \right\rangle \right]$, where $\alpha = 1, 2, 3$ represents the three sublattices of the 120° order. The second is the square sublattice magnetization for the stripe phases [23, 26]: $m_{str}^2 = \frac{1}{6} \sum_{v=1}^3 \sum_{\beta_v=1}^2 \left[\frac{1}{(N/4)(N/4+1)} \left\langle \left(\sum_{i \in \beta_v} \mathbf{S}_i \right)^2 \right\rangle \right]$, where $v = 1, 2, 3$ represents three kinds of stripe orders, and $\beta_v = 1, 2$ represents the two sublattices of v -kind stripe order. We use the leading linear scaling $1/\sqrt{N}$ to estimate the magnetic orders in the thermodynamic limit. The finite-size clusters used in the ED calculations are shown in Supplemental Material.

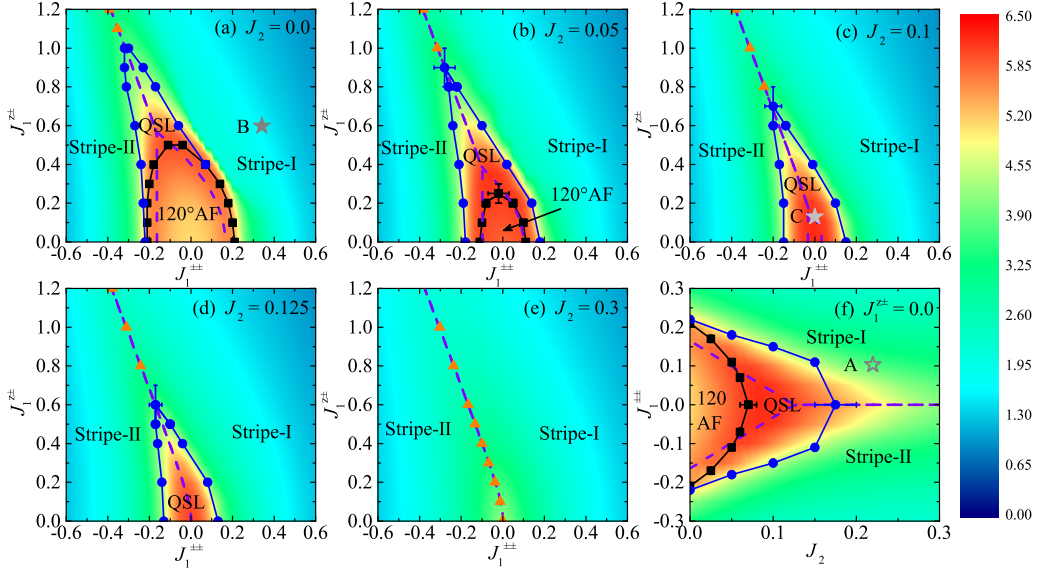


FIG. 2. Phase diagrams on the slices of (a) $J_2 = 0, J_1^{\pm\pm} - J_1^{z\pm}$; (b) $J_2 = 0.05, J_1^{\pm\pm} - J_1^{z\pm}$; (c) $J_2 = 0.1, J_1^{\pm\pm} - J_1^{z\pm}$; (d) $J_2 = 0.125, J_1^{\pm\pm} - J_1^{z\pm}$; (e) $J_2 = 0.3, J_1^{\pm\pm} - J_1^{z\pm}$ and (f) $J_1^{z\pm} = 0, J_2 - J_1^{\pm\pm}$. The color bar shows the strength of frustration parameter f obtained by full exact diagonalization using 12-site cluster. The black and blue phase transition points are obtained from linear extrapolations of finite-size magnetic order parameters, while the yellow points are obtained by the level crossings of low excited energy states (see FIG. 5). The purple dashed lines are the classical phase transition lines between three magnetic phases. The star points A, B and C shown in (f), (a) and (c) denote some sets of exchange parameters fitted by experimental data and get from Ref. 7, Ref. 24 and Ref. 27, respectively. The hollow star point A used a different easy-plane anisotropic $\alpha \approx 1.73$. Some sets of exchange parameters are summarized in Ref. 28.

Phase diagram The 3D phase diagram was shown in FIG. 1. Inside the dark yellow curved surface is the 120° Néel phase. In between the dark yellow curved surface and the green curved surface is a quantum spin liquid phase region. This region is a QSL based on two main reasons: one is that there is no conventional orders; another is that this phase is adiabatically connected to the QSL phase in the $J_1 - J_2$ triangular Heisenberg model.

And the light yellow curved surface separates Stripe-I and Stripe-II phases. We do not observe any multi-Q phase as in the classical Monte Carlo simulation [14] based on that the spin structure factors do not have sharp peaks at the momentum points other than two K points and three M points in different clusters. To see more details of this 3D phase diagram, we plot some slices in FIG. 2. The QSL boundaries are obtained by the van-

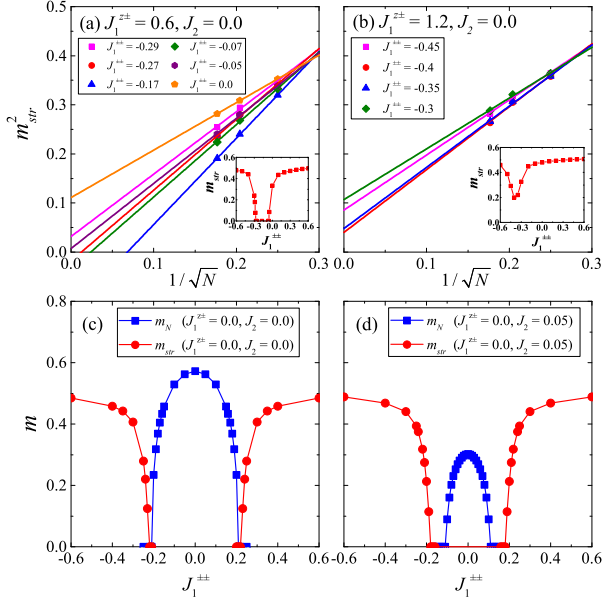


FIG. 3. Linear extrapolations of the square sublattice magnetization for the stripe orders in selective paths which go along (a) $J_1^{z\pm} = 0.6$ and (b) $J_1^{z\pm} = 1.2$ horizontal lines in the phase slice of FIG. 2(a). The extrapolated stripe orders are shown in the insets. When $J_1^{z\pm} = 0.6$, there are two phase transition points at around $J_{1c}^{z\pm} \approx -0.28$ and $J_{1c}^{z\pm} \approx -0.05$. While for $J_1^{z\pm} = 1.2$, the extrapolated stripe order has a minimum at around $J_{1c}^{z\pm} \approx -0.39$ which is a signature of the first-order transition between two stripe phases and is nearly the same as the classical transition point. (c) and (d) are the extrapolated magnetic orders along $J_1^{z\pm} = 0$ horizontal lines in FIG. 2(a) and FIG. 2(b), respectively. The 120° Néel phase (blue, square) is sandwiched by two stripe phases (red, circle) at $J_2 = 0$. While at $J_2 = 0.05$, the QSL phase extends to the $J_1^{z\pm} = 0.0$ region.

ishing of two kinds of magnetic orders: 120° Néel order and stripe order. Some detailed extrapolations can be seen in Supplemental Material. In FIG. 3, we representatively show the linear extrapolations of magnetic orders along some paths in some 2D slices. In addition, in FIG. 2, we use contour plot to show the frustration parameter $f = |\Theta_{CW}|/T_c$ in the slices, where Θ_{CW} is the negative Curie-Weiss temperature and T_c is the critical temperature. Here, we take the T_c approximately as the temperature where the heat capacity gets its maximum value. We can observe that the QSL region have a larger frustration parameter, especially after adding the next-nearest-neighbor J_2 interaction. The strong frustration in these regions prevent the magnetic ordering even at zero temperature. Under the guidance of the 3D phase diagram, we compare different sets of exchange parameters obtained by different research groups. Most of the parameter sets fall into the stripe phases. We only show three of them which is within or close to the QSL region, labeled with A, B and C in FIG. 2. Here we want to mention that the anisotropic exchange inter-

actions $J_1^{\pm\pm}$ and $J_1^{z\pm}$ are weaker effects from the ESR measurement. However, from our ED calculations, we find that the QSL region with only nearest-neighbor interactions needs a large $J_1^{z\pm} \sim 0.5J_1$, but it would be reduced by adding the next-nearest-neighbor interaction or decreasing the XXZ anisotropic α , which means J_2 is important to capture spin-liquid-behavior of YbMgGaO₄ material if one has to neglect the possible chemical disorders and let $\alpha \sim 1$. Compared to previous DMRG result from Ref. 19, though different α is used, our QSL region in the $J_1^{\pm\pm} - J_1^{z\pm}, J_2 = 0$ plane is different to the DMRG one which is within the conelike shape of 120° Néel ordered phase region. If we take a line path which connects two QSL regions in the $J_1^{\pm\pm} - J_1^{z\pm}, J_2 = 0$ and $J_2 - J_1^{\pm\pm}, J_1^{z\pm} = 0$ planes, we observe that the static spin structure factors $S(\mathbf{q})$ always have broad peaks at around M points, not at the K points observed in Ref. 19.

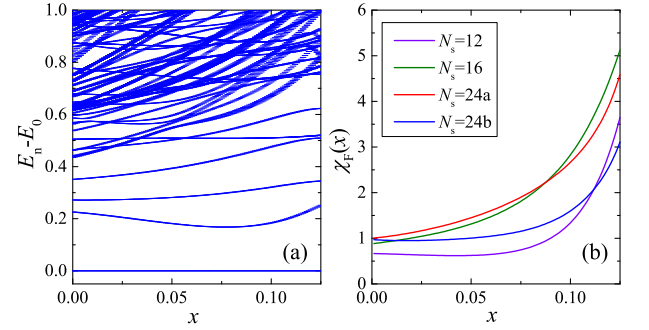


FIG. 4. (a) Low energy spectrum obtained by the 24a cluster and (b) fidelity susceptibility of different clusters change with control parameter x (see the main text for details). No level crossing or quasi-degeneracy has been found by different clusters. And there is no any peak structure among $x \in [0.0, 0.125]$ in the fidelity susceptibility. The increasing behavior near $x = 0.125$ only indicates that it is close to the phase transition point between stripe phase and QSL.

Quantum spin liquid To give a better understanding of the nonmagnetic phase, we have also calculated the chiral and dimer structure factors [23] and got the vanishing extrapolated values. In addition, we have calculated the spin freezing order parameter $\bar{q} = \frac{1}{N} \sqrt{\sum_{ij} [\langle \hat{\mathbf{S}}_i \hat{\mathbf{S}}_j \rangle^2]}$ to detect the possible spin glass order. It also goes to zero within linear extrapolation. Therefore, there is no magnetic orders, chiral order, valence-bond-solid order and spin-glass order in the nonmagnetic region which may be a quantum spin liquid phase. Actually, according to the previous numerical and theoretical studies [29–36], a quantum spin liquid phase in $J_1 - J_2$ triangular Heisenberg model is sandwiched between the 120° Néel phase and the stripe phase. In our case with easy-plane anisotropy, the quantum spin liquid region with $J_1^{\pm\pm} = 0, J_1^{z\pm} = 0$ shown in FIG. 2(f) is about $0.07 < J_2 < 0.175$. After adding the $J_1^{\pm\pm}$ interaction,

this region of quantum spin liquid phase shrinks, but extends to the $J_2 = 0, J_1^{\pm\pm} \sim \pm 0.2$. To show whether the nonmagnetic phase in the $J_2 = 0, J_1^{\pm\pm} - J_1^{z\pm}$ plane and the quantum spin liquid phase in the $J_1^{z\pm} = 0, J_2 - J_1^{\pm\pm}$ plane is the same phase, we use low energy spectrum and ground state wavefunction to detect the possible gap closing or the sudden change of fidelity susceptibility. The fidelity $F(x) = |\langle \Psi_0(x) | \Psi_0(x + \delta x) \rangle|$ measures the amounts of shared information between two quantum states. If there is a quantum phase transition, a singularity will develop in the fidelity susceptibility defined as $\chi_F(x) = \frac{2[1-F(x)]}{N(\delta x)^2}$. Here, we take a straight-line path $J_2 = x, J_1^{\pm\pm} = 1.6x - 0.2, J_1^{z\pm} = -5.6x + 0.7, x \in [0, 0.125]$ in the 3D parameter space to show the low energy spectrum and the fidelity susceptibility. From the low energy spectra of finite-size clusters, no any level crossing or avoided level crossing occurs. From the ground-state fidelity susceptibility shown in FIG. 4, we do not observe any discontinuity or divergent tendency as footprints of quantum phase transition. We believe that there would be no quantum phase transition between two nonmagnetic regions in the thermodynamic limit. And they belong to the same quantum spin liquid phase which is consistent with previous DMRG study [19]. When $J_2 = 0$, the quantum spin liquid phase is surrounded by two stripe phases and the 120° Néel phase. After adding J_2 , the 120° Néel phase is suppressed, while the area of QSL phase increases first, and then starts to drop, eventually disappears, see FIG. 2(a-e). In addition, we do not see any quasi-degenerate states in the QSL region from our finite-size calculations. We conjecture that this QSL would be gapless in the thermodynamic limit similar to the $J_1 - J_2$ triangular Heisenberg model [21, 35, 36].

Two stripe phases Next, we want to discuss the stripe-I and stripe-II phases. From the low energy spectra of finite-size clusters shown in FIG. 5, we can conclude that Stripe-I and Stripe-II phases are Ising-like phases that have six degenerate ground states and a finite excitation gap. This degeneracy will be lifted after spontaneously Z_6 discrete symmetry breaking below a finite critical temperature T_c in the thermodynamic limit [20].

Magnetic field effects Applying magnetic field is a useful technique to probe the magnetic system. We have studied the magnetization curves of three magnetic ordered phases and the quantum spin liquid phase. Here in the main text, we only show the magnetization curves at $J_1^{\pm\pm} = -0.17, J_1^{z\pm} = 0.6, J_2 = 0.0$ of QSL region with the magnetic field applied perpendicular to the c axis. Though there are finite-size effects, we still can observe a clear “melting” 1/3-magnetization plateau. This 1/3-plateau or “*uud*” phase is widely observed in triangular-lattice antiferromagnetic materials. The nonflatness of this plateau at zero temperature is due to the out of xy plane anisotropic interaction $J_1^{z\pm}$. When the $J_1^{z\pm}$ further increases in the QSL region, this plateau melts to nonlin-

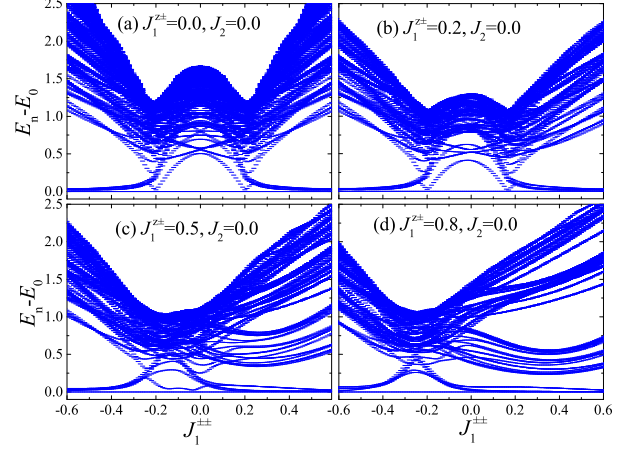


FIG. 5. Low energy spectra of 24a cluster with nearest-neighbor anisotropic interactions. There are six degenerate ground states and a finite excitation gap in the stripe-I and stripe-II phase regions. The “inverse V-shape” in the low energy spectra is more clear when $J_1^{z\pm}$ becomes larger. And the tip of “inverse V-shape” can be used to determine the direct (first-order) phase transition points between two stripe phases on different slices [see the yellow triangular point in FIG. 2].

ear rough curve. Another contribution to the nonflatness of the plateau is the temperature. When the temperature increases, the plateau will further melt to become rough curve. At sufficient high temperature, it becomes a linear curve, which is shown in the inset of FIG. 6 (a). For the spin structure factor $S(\mathbf{q})$, we can observe that the spectral weight shifts from M points in the zero field to the K points in the sufficient strong field around the 1/3-magnetization plateau, and then transfers to the Γ point in the fully polarized region. Interestingly, the recent experiment on the YbMgGaO_4 [27] with very low temperature has discovered the non-linearity in the magnetization curve which may be a signature of the remnant of 1/3-magnetization plateau, and it may be seen more clear if further lowering the temperature. The DMRG and classical Monte Carlo simulations using the C set of parameters [see Fig. 2 (c)] have reproduced the non-linearity of magnetization curve. Here, our ED method have reproduced the similar behaviors not only in the C set of parameters but also in large region of QSL phase. What’s more, adding J_2 do not obviously change the flatness of the plateau, but the interval of the plateau will shrink [37]. In addition, we have also studied the magnetization curves with the magnetic field parallel to the c axis. The 1/3-magnetization plateau seems still visible at $J_1^{\pm\pm} = -0.17, J_1^{z\pm} = 0.6, J_2 = 0.0$, but has a quite narrow interval which is due to the easy-plane anisotropy α and the out of plane anisotropic interactions $J_1^{z\pm}$. More details about the magnetization curves of different phases can be seen in Supplemental Material.

Bond randomness effects To study the possible chem-

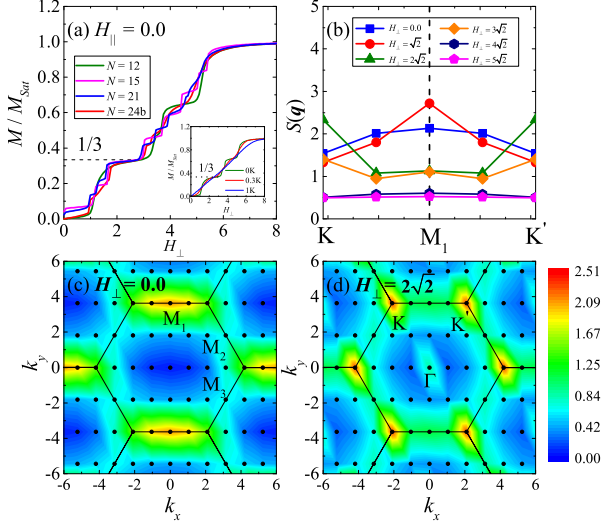


FIG. 6. (a) Magnetization curves of the quantum spin liquid phase at $J_1^{\pm\pm} = -0.17$, $J_1^{z\pm} = 0.6$, $J_2 = 0.0$ under external magnetic field applied perpendicular to the c axis. Combined the results of different clusters, a “melting” $1/3$ magnetization plateau is clearly shown near $H_{\perp} = 2.5$. The inset shows the temperature dependence of magnetization curves obtained by 12-site cluster. (b) The spin structure factors $S(\mathbf{q})$ along $K \rightarrow M_1 \rightarrow K'$ high symmetry path in the Brillouin zone (BZ) under different magnetic fields. With the increasing magnetic field, the spectral weight shifts from M points in the zero field to the K points around the plateau and then transfers to Γ point in the fully polarized phase. (c) and (d) are the contour plots of static spin structure factors in the whole BZ at $H_{\perp} = 0$ and $2\sqrt{2}$, respectively. We use the 24b cluster to get those results in (b), (c) and (d).

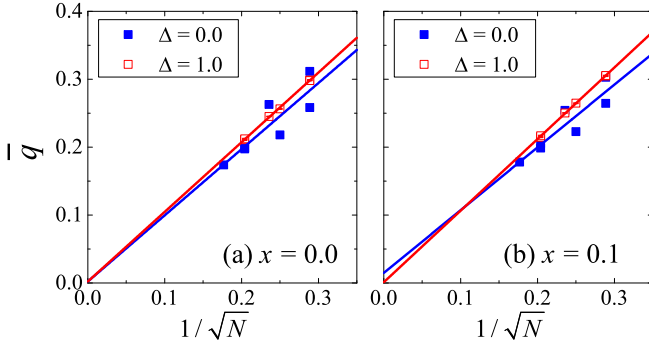


FIG. 7. The spin freezing order parameters \bar{q} in the clean and strongest bond randomness cases. Almost zero extrapolated values indicate there is no spin glass order. We have used at least 50 bond-randomness samples to get the average \bar{q} .

ical disorders in real materials, like Ga/Mg mixing in YbMgGaO_4 , we add uniform bond randomness into the Hamiltonian and mainly discuss the ground state properties in the main text. Other distributions of the random exchange interactions do not change the conclusion qualitatively. For two stripe phases with finite excitation

gaps, the magnetic orders are very stable to the bond randomness and persist up to the strongest randomness $\Delta = 1$. For the 120° Néel order, it is fragile to bond randomness but can persist up to a critical bond randomness strength $\Delta_c < 1$ according to previous ED and DMRG study [23]. So in the strongest bond randomness $\Delta = 1$ case, not only the QSL region but also the stripe phase regions which are very close to the phase boundaries and the whole 120° phase region will show nonmagnetic spin-liquid-like behavior. To detect the possible spin-glass order induced by the bond randomness, we show the spin freezing parameter in FIG. 7. Both in the clean and bond randomness cases, they all are extrapolated to zero. There would be no spin glass order even in the strongest bond randomness case. It may be a 2D random singlet (RS) phase after adding sufficient strong bond randomness in the 120° phase and the QSL phase regions [38]. More discussions about the bond randomness effects on the stripe-I phase at finite temperature can be seen in Supplemental Material. As for the magnetization curve, the $1/3$ -magnetization plateau will further melt by the randomness of exchange interactions and g -factors [25], similar to the temperature effect.

Summary and discussion In summary, we have used ED calculations to get the whole phase diagram in the 3D parameter space. Besides two gapped stripe phases and 120° Néel phase, there is a large nonmagnetic region extending to the quantum spin liquid phase in the $J_1 - J_2$ triangular Heisenberg model. Using extensive finite-size scaling, we get the concrete phase boundaries. After applying external magnetic fields, the $1/3$ -magnetization plateau can be observed at large region of QSL phase when the magnetic field is perpendicular to the c axis. In addition, we explore the bond randomness effects. Numerical results show no glass ordering both in the 120° Néel phase and the quantum spin liquid phase. It may be a 2D analog of random-singlet phase in the strongest bond randomness case. Its nature is still a challenge task that leaves for future study.

Acknowledgments H.Q.W. would like to thank Shou-Shu Gong, Wei Zhu, and Rong-Qiang He for helpful discussions. We would like to thank Zhiyao Ning for helping drawing the FIG. 1 using Matlab. The numerical calculations were carried out at the National Supercomputer Center in Guangzhou on the Tianhe-2 platform. D.X.Y. is supported by NKRDPC-2018YFA0306001, NKRDPC-2017YFA0206203, NSFC-11974432, GBABRF-2019A1515011337, and Leading Talent Program of Guangdong Special Projects. H.Q.W. is supported by the National Natural Science Foundation of China through Grant No. 11804401 and the Fundamental Research Funds for the Central Universities.

* yaodaox@mail.sysu.edu.cn

† wuhangq3@mail.sysu.edu.cn

- [1] X. G. Wen, *Phys. Rev. B* **44**, 2664 (1991); L. Balents, *Nature* **464**, 199 (2010); X.-G. Wen, *Phys. Rev. B* **65**, 165113 (2002); A. Kitaev, *Annals of Physics* **321**, 2 (2006); L. Savary and L. Balents, *Rep. Prog. Phys.* **80**, 016502 (2016); M. R. Norman, *Rev. Mod. Phys.* **88**, 041002 (2016); Y. Zhou, K. Kanoda, and T.-K. Ng, *Rev. Mod. Phys.* **89**, 025003 (2017); C. Broholm, R. J. Cava, S. A. Kivelson, D. G. Nocera, M. R. Norman, and T. Senthil, *Science* **367** (2020), 10.1126/science.aay0668.
- [2] Y. Li, H. Liao, Z. Zhang, S. Li, F. Jin, L. Ling, L. Zhang, Y. Zou, L. Pi, Z. Yang, J. Wang, Z. Wu, and Q. Zhang, *Scientific Reports* **5**, 16419 (2015).
- [3] Y. Li, G. Chen, W. Tong, L. Pi, J. Liu, Z. Yang, X. Wang, and Q. Zhang, *Phys. Rev. Lett.* **115**, 167203 (2015).
- [4] Y. Li, D. Adroja, P. K. Biswas, P. J. Baker, Q. Zhang, J. Liu, A. A. Tsirlin, P. Gegenwart, and Q. Zhang, *Phys. Rev. Lett.* **117**, 097201 (2016).
- [5] Y. Li, D. Adroja, R. I. Bewley, D. Voneshen, A. A. Tsirlin, P. Gegenwart, and Q. Zhang, *Phys. Rev. Lett.* **118**, 107202 (2017).
- [6] Y. Shen, Y.-D. Li, H. Wo, Y. Li, S. Shen, B. Pan, Q. Wang, H. C. Walker, P. Steffens, M. Boehm, Y. Hao, D. L. Quintero-Castro, L. W. Harriger, M. D. Frontzek, L. Hao, S. Meng, Q. Zhang, G. Chen, and J. Zhao, *Nature* **540**, 559 (2016).
- [7] J. A. M. Paddison, M. Daum, Z. Dun, G. Ehlers, Y. Liu, M. B. Stone, H. Zhou, and M. Mourigal, *Nat. Phys.* **13**, 117 (2016).
- [8] Y. Li, S. Bachus, B. Liu, I. Radelytskyi, A. Bertin, A. Schneidewind, Y. Tokiwa, A. A. Tsirlin, and P. Gegenwart, *Phys. Rev. Lett.* **122**, 137201 (2019).
- [9] W. Liu, Z. Zhang, J. Ji, Y. Liu, J. Li, X. Wang, H. Lei, G. Chen, and Q. Zhang, *Chin. Phys. Lett.* **35**, 117501 (2018).
- [10] Y. Shen, Y.-D. Li, H. C. Walker, P. Steffens, M. Boehm, X. Zhang, S. Shen, H. Wo, G. Chen, and J. Zhao, *Nat. Comm.* **9**, 4138 (2018).
- [11] P.-L. Dai, G. Zhang, Y. Xie, C. Duan, Y. Gao, Z. Zhu, E. Feng, C.-L. Huang, H. Cao, A. Podlesnavak, G. E. Granroth, D. Voneshen, S. Wang, G. Tan, E. Morosan, X. Wang, L. Shu, G. Chen, Y. Guo, X. Lu, and P. Dai, *arXiv* **2004**, 06867 (2020).
- [12] Z. Ma, J. Wang, Z.-Y. Dong, J. Zhang, S. Li, S.-H. Zheng, Y. Yu, W. Wang, L. Che, K. Ran, S. Bao, Z. Cai, P. Čermák, A. Schneidewind, S. Yano, J. S. Gardner, X. Lu, S.-L. Yu, J.-M. Liu, S. Li, J.-X. Li, and J. Wen, *Phys. Rev. Lett.* **120**, 087201 (2018).
- [13] Y.-D. Li, X. Wang, and G. Chen, *Phys. Rev. B* **94**, 035107 (2016).
- [14] C. Liu, R. Yu, and X. Wang, *Phys. Rev. B* **94**, 174424 (2016).
- [15] Y.-D. Li, Y.-M. Lu, and G. Chen, *Phys. Rev. B* **96**, 054445 (2017).
- [16] Y.-D. Li and G. Chen, *Phys. Rev. B* **96**, 075105 (2017).
- [17] Q. Luo, S. Hu, B. Xi, J. Zhao, and X. Wang, *Phys. Rev. B* **95**, 165110 (2017).
- [18] Z. Zhu, P. A. Maksimov, S. R. White, and A. L. Chernyshev, *Phys. Rev. Lett.* **119**, 157201 (2017).
- [19] Z. Zhu, P. A. Maksimov, S. R. White, and A. L. Chernyshev, *Phys. Rev. Lett.* **120**, 207203 (2018).
- [20] E. Parker and L. Balents, *Phys. Rev. B* **97**, 184413 (2018).
- [21] J. Iaconis, C. Liu, G. B. Halasz, and L. Balents, *SciPost Phys.* **4**, 003 (2018).
- [22] P. A. Maksimov, Z. Zhu, S. R. White, and A. L. Chernyshev, *Phys. Rev. X* **9**, 021017 (2019).
- [23] H.-Q. Wu, S.-S. Gong, and D. N. Sheng, *Phys. Rev. B* **99**, 085141 (2019).
- [24] Y.-D. Li, Y. Shen, Y. Li, J. Zhao, and G. Chen, *Phys. Rev. B* **97**, 125105 (2018).
- [25] K. Watanabe, H. Kawamura, H. Nakano, and T. Sakai, *Journal of the Physical Society of Japan* **83**, 034714 (2014).
- [26] T. Shimokawa, K. Watanabe, and H. Kawamura, *Phys. Rev. B* **92**, 134407 (2015).
- [27] W. M. Steinhardt, Z. Shi, A. Samarakoon, S. Disanayake, D. Graf, Y. Liu, W. Zhu, C. Marjerrison, C. D. Batista, and S. Haravifard, *arXiv* **1902**, 07825 (2019).
- [28] X. Zhang, F. Mahmood, M. Daum, Z. Dun, J. A. M. Paddison, N. J. Laurita, T. Hong, H. Zhou, N. P. Armitage, and M. Mourigal, *Phys. Rev. X* **8**, 031001 (2018).
- [29] R. Kaneko, S. Morita, and M. Imada, *Journal of the Physical Society of Japan* **83**, 093707 (2014).
- [30] P. H. Y. Li, R. F. Bishop, and C. E. Campbell, *Phys. Rev. B* **91**, 014426 (2015).
- [31] Z. Zhu and S. R. White, *Phys. Rev. B* **92**, 041105 (2015).
- [32] W.-J. Hu, S.-S. Gong, W. Zhu, and D. N. Sheng, *Phys. Rev. B* **92**, 140403 (2015).
- [33] Y. Iqbal, W.-J. Hu, R. Thomale, D. Poilblanc, and F. Becca, *Phys. Rev. B* **93**, 144411 (2016).
- [34] S. N. Saadatmand and I. P. McCulloch, *Phys. Rev. B* **94**, 121111 (2016).
- [35] S. Hu, W. Zhu, S. Eggert, and Y.-C. He, *Phys. Rev. Lett.* **123**, 207203 (2019).
- [36] F. Ferrari and F. Becca, *Phys. Rev. X* **9**, 031026 (2019).
- [37] H. Nakano and T. Sakai, *Journal of the Physical Society of Japan* **86**, 114705 (2017).
- [38] I. Kimchi, A. Nahum, and T. Senthil, *Phys. Rev. X* **8**, 031028 (2018).
- [39] M. Baenitz, P. Schlender, J. Sichelschmidt, Y. A. Onyukienko, Z. Zangeneh, K. M. Ranjith, R. Sarkar, L. Hozoi, H. C. Walker, J.-C. Orain, H. Yasuoka, J. van den Brink, H. H. Klauss, D. S. Inosov, and T. Doert, *Phys. Rev. B* **98**, 220409 (2018).
- [40] K. M. Ranjith, D. Dmytriieva, S. Khim, J. Sichelschmidt, S. Luther, D. Ehlers, H. Yasuoka, J. Wosnitza, A. A. Tsirlin, H. Kühne, and M. Baenitz, *Phys. Rev. B* **99**, 180401 (2019).
- [41] L. Ding, P. Manuel, S. Bachus, F. Grubler, P. Gegenwart, J. Singleton, R. D. Johnson, H. C. Walker, D. T. Adroja, A. D. Hillier, and A. A. Tsirlin, *Phys. Rev. B* **100**, 144432 (2019).
- [42] J. Guo, X. Zhao, S. Ohira-Kawamura, L. Ling, J. Wang, L. He, K. Nakajima, B. Li, and Z. Zhang, *Phys. Rev. Materials* **4**, 064410 (2020).
- [43] M. M. Bordelon, C. Liu, L. Posthuma, P. M. Sarte, N. P. Butch, D. M. Pajerowski, A. Banerjee, L. Balents, and S. D. Wilson, *Phys. Rev. B* **101**, 224427 (2020).
- [44] M. M. Bordelon, E. Kenney, C. Liu, T. Hogan, L. Posthuma, M. Kavand, Y. Lyu, M. Sherwin, N. P. Butch, C. Brown, M. J. Graf, L. Balents, and S. D. Wilson, *Nat. Phys.* **15**, 1058 (2020).

Supplemental Material: Exact diagonalization study of the anisotropic Heisenberg model related to YbMgGaO₄

Muwei Wu, Dao-Xin Yao*, Han-Qing Wu†

*State Key Laboratory of Optoelectronic Materials and Technologies,
School of Physics, Sun Yat-Sen University, Guangzhou, 510275, China*

I. FINITE-SIZE CLUSTERS USED IN THE ED CALCULATIONS

In this paper, we mainly use Lanczos exact diagonalization to get the 3D phase diagram and the low energy spectrum. Meanwhile, we also employ full exact diagonalization to study the finite-temperature properties, such as heat capacity and magnetic susceptibility. To reduce the computational cost, we have used translation symmetry to do block diagonalization. The largest system size in the Lanczos calculations is 32 with the subspace of the largest block up to 0.13 billion.

Seven clusters are mainly used in our ED calculations which are shown in FIG. 8, denoted as 12, 15, 16, 18, 21, 24a, 24b, 24c and 32, respectively. The 12, 16, 24a, 24b and 32 clusters have three M momentum points which are significant for the stripe phases. These three momentum points denote as $M_1 = \frac{1}{2}b_2$, $M_2 = \frac{1}{2}(b_1 + b_2)$, $M_3 = \frac{1}{2}b_1$, where $b_1 = (\frac{2\pi}{a}, -\frac{2\pi}{\sqrt{3}a})$, $b_2 = (0, \frac{4\pi}{\sqrt{3}a})$ are primitive lattice vectors in reciprocal space, $a = 1$ is the lattice constant. Among these five clusters with even number of lattice site, the 12 and 24b clusters also contain two K points, $K_1 = \frac{1}{3}b_1 + \frac{2}{3}b_2$, $K_2 = \frac{2}{3}b_1 + \frac{1}{3}b_2$. The K points are important for 120° Néel phase and the 1/3-magnetization plateau phase or “*uud*” phase. So we use the 12, 15, 18, 21, 24b and 24c clusters which contain K points to do the linear extrapolations of 120° Néel order and to study the 1/3-magnetization plateau.

Here, we want to mention that three M momentum points are nonequivalent in the 24a, 24b and 32 clusters. Therefore, there may be only one M point which has broad peak in the spin structure factor $S(\mathbf{q})$ of QSL region [see FIG.6 (c) in the main text and FIG. 11 (a2-d2)]. We should see the diffuse magnetic scattering at around all three M points when we use the clusters which have equivalent M points, such as 16 and 36 clusters [see FIG. 11 (a2-d2)].

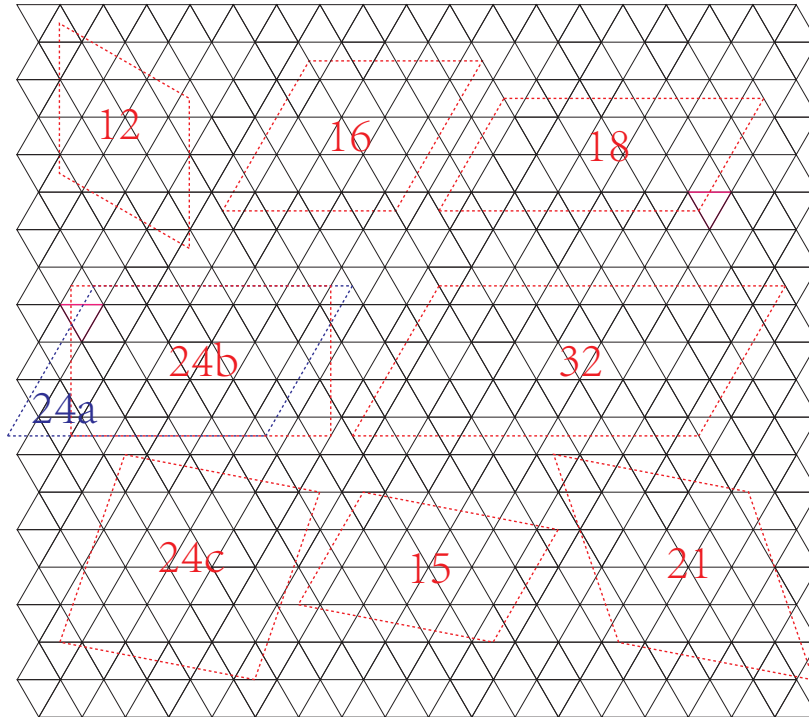


FIG. 8. Finite-size clusters used in the ED calculations. The 12 cluster has been used to do the full exact diagonalization and calculate the frustration parameter.

II: EXTRAPOLATIONS OF CONVENTIONAL ORDERS

We have representatively shown the linear extrapolations of 120° Néel order and the stripe orders in the main text. Here, we want to show more details about the extrapolations, which are shown in FIG. 9. The magnetic order parameters (square root of the extrapolated results) obtained from FIGs. 9(a1),9(b1),9(a2) and 9(b2) are shown in FIGs. 3(c) and 3(d) in the main text.

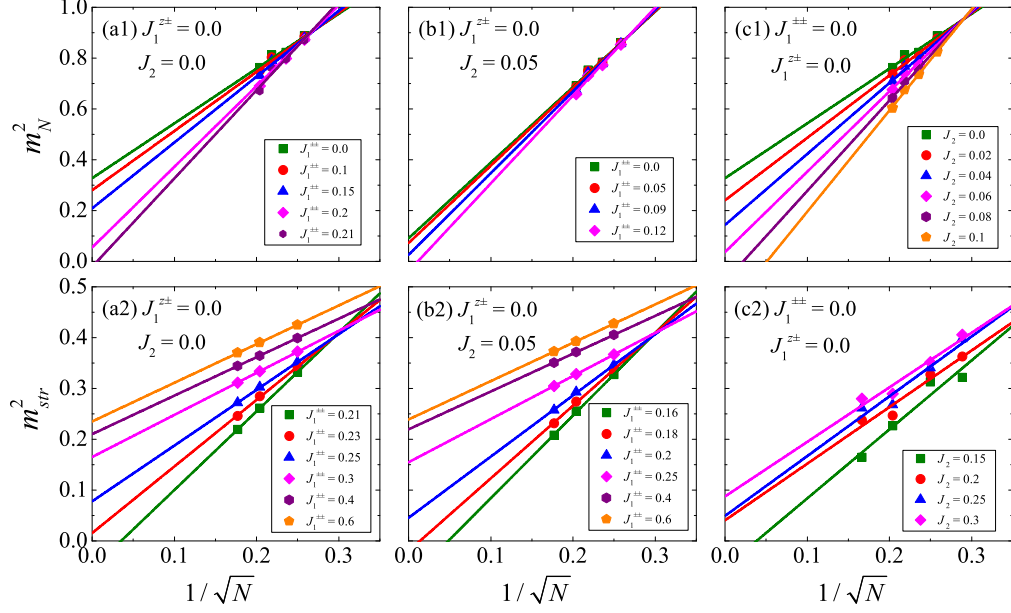


FIG. 9. The linear extrapolations of the square sublattice magnetizations for (a1-c1) the 120° Néel phase and (a2-c2) the stripe phases.

Here, we mention that the stripe phases are Ising-like phase which have strong magnetic orders and weaker quantum fluctuations. Therefore, the linear extrapolations of magnetic orders are good enough to identify the phase boundaries. The extrapolated results will not change much when using some larger system sizes.

To eliminate other conventional orders in the nonmagnetic phase region, we have also calculated the chiral and dimer structure factors which are defined in the following,

$$\chi(\mathbf{q}) = \frac{1}{N} \sum_{ij} e^{-i\mathbf{q}\mathbf{r}_{ij}} [\langle \hat{\chi}_i \hat{\chi}_j \rangle], \hat{\chi}_i = \hat{\mathbf{S}}_i \cdot (\hat{\mathbf{S}}_{i+\mathbf{a}_1} \times \hat{\mathbf{S}}_{i+\mathbf{a}_2}),$$

$$D(\mathbf{q}) = \frac{1}{3N} \sum_{ij} \sum_{pq} e^{-i\mathbf{q}\mathbf{r}_{ip,jq}} [\langle \hat{\mathbf{B}}_{ip} \hat{\mathbf{B}}_{jq} \rangle], \hat{\mathbf{B}}_{ip} = \hat{\mathbf{S}}_i \hat{\mathbf{S}}_{i+p} - \langle \hat{\mathbf{S}}_i \hat{\mathbf{S}}_{i+p} \rangle,$$

where $i+p$ means the nearest-neighbor site of i -site along $\mathbf{a}_1, \mathbf{a}_2, -\mathbf{a}_1 + \mathbf{a}_2$ direction for $p = 1, 2, 3$ respectively. $\mathbf{a}_1 = (1, 0)$ and $\mathbf{a}_2 = (\frac{1}{2}, \frac{\sqrt{3}}{2})$ are the primitive vectors of the triangular lattice. $\mathbf{r}_{ip,jq}$ means the displacement between centers of two bonds. From the finite-size calculations obtained by $24a$ cluster, a stripe-like pattern and a peak at the Γ point are observed in the chiral and dimer structure factors, respectively, see FIGs. 10 (c) and (d). From finite-size scalings using the maxima of $\chi(\mathbf{q})$ and $D(\mathbf{q})$, we got negative extrapolated values of both orders which indicate the absence of chiral and dimer orders in the QSL phase, see FIGs. 10 (a) and (b). Therefore, the large region of nonmagnetic phase in the 3D parameter space has no 120° Néel order, stripe orders, chiral order and dimer order, and it could be a quantum spin liquid phase. Actually, this nonmagnetic phase is adiabatically connected to the QSL phase in the $J_1 - J_2$ triangular Heisenberg model.

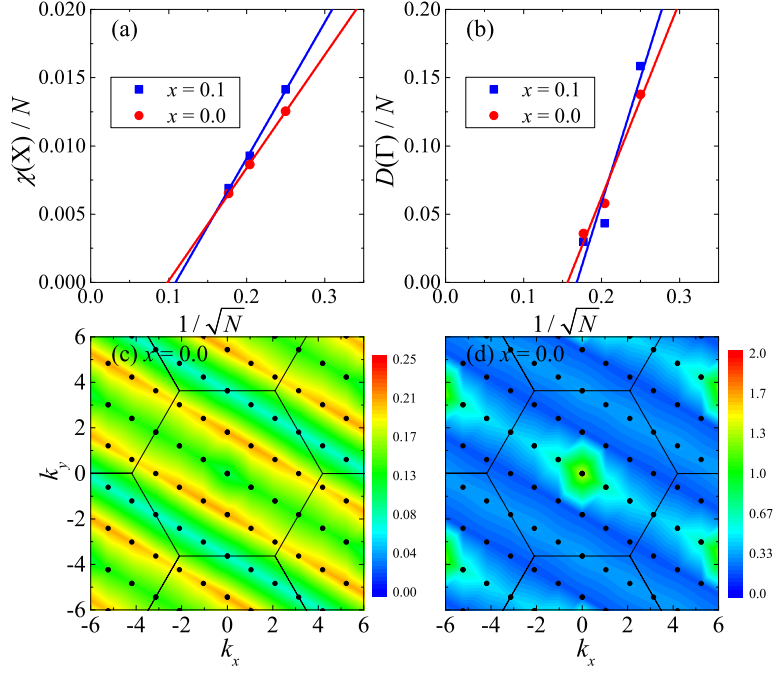


FIG. 10. The linear extrapolations of (a) chiral structure factors $\chi(X)$ and (b) dimer structure factors $D(\Gamma)$ at $x = 0.1$ and $x = 0.0$, X is the momentum point where $\chi(\mathbf{q})$ gets its maximum. (c) and (d) are the contour plot of chiral structure factor $\chi(\mathbf{q})$ and dimer structure factor $D(\mathbf{q})$ at $x = 0.0$, respectively. x specifies the exchange interactions $J_2 = x$, $J_1^{\pm\pm} = 1.6x - 0.2$, $J_1^{z\pm} = -5.6x + 0.7$, $x \in [0, 0.125]$.

The inelastic neutron scattering experiment of YbMgGaO_4 has revealed a broad low-energy excitation maxima at the M point and the concentrated spectral weight at the boundary of Brillouin zone. Here, we show the contour plots of spin structure factor in the QSL region which is show in FIG. 11. We take a straight-line path $J_2 = x$, $J_1^{\pm\pm} = 1.6x - 0.2$, $J_1^{z\pm} = -5.6x + 0.7$, $x \in [0, 0.125]$ in the 3D parameter space to show the spin structure factor of QSL phase. The broad peaks at the M points signature short-range stripe-like spin correlations in the QSL phase which is consistent with experiment.

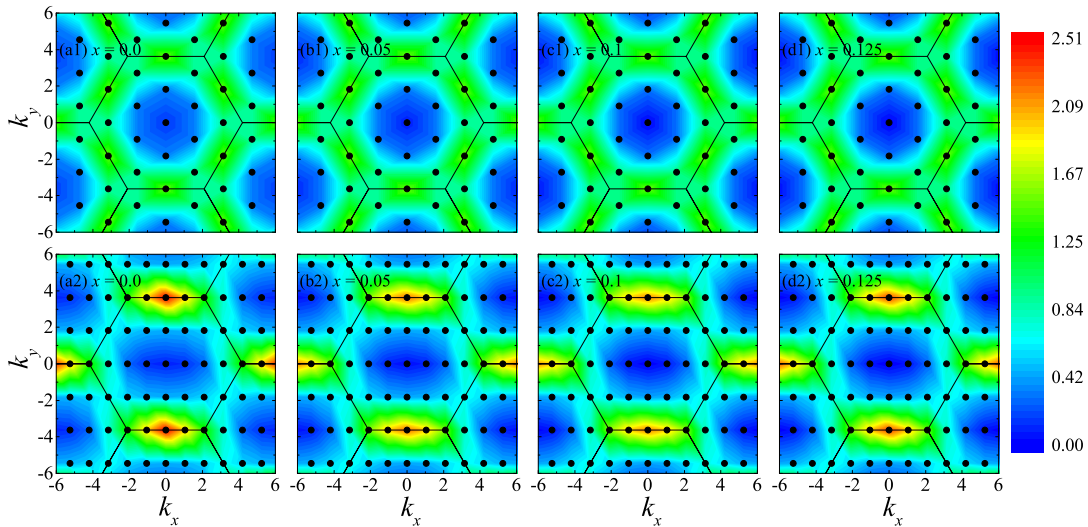


FIG. 11. Spin structure factors at different x . x specifies the exchange interactions $J_2 = x$, $J_1^{\pm\pm} = 1.6x - 0.2$, $J_1^{z\pm} = -5.6x + 0.7$, $x \in [0, 0.125]$. (a1-d1) are obtained by 16 cluster, while (a2-d2) are obtained by 24b cluster.

III. STRIPE-I AND STRIPE-II PHASES

In the main text, we have calculated the low energy spectra of different phases and find that there are six degenerate ground states in the stripe phases (see FIG.5 in the main text). These six degenerate ground states are in the translation invariant momentum sectors Γ, M_1, M_2, M_3 . Three of them are in the Γ sector, while the other three distribute into three M sectors. We can use finite-size scaling of energy gaps to verify the degeneracy in the thermodynamic limit which is shown in FIG. 12.

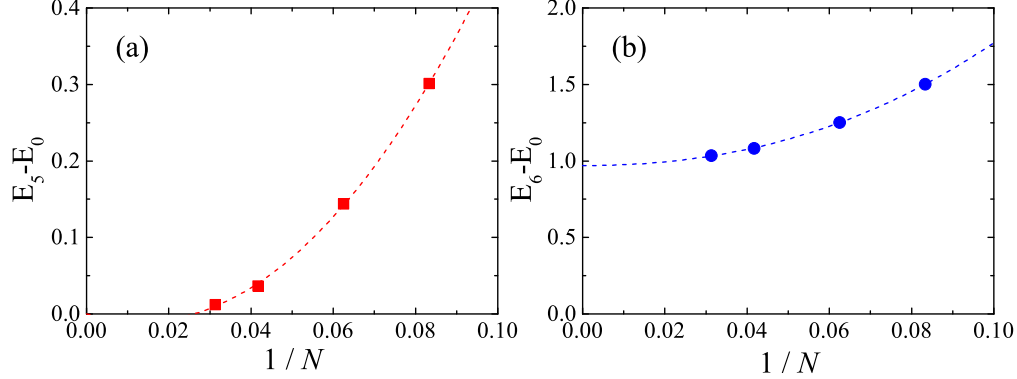


FIG. 12. (a) The third order polynomial extrapolations of (a) the finite-size gap of the six ground state manifolds (GSM) and (b) the excitation gap above the GSM at $J_1^{\pm\pm} = 0.6, J_1^{z\pm} = 0, J_2 = 0$ [see FIG. 5(a) in the main text].

Previous study from Ref. 20 has shown that there are six basic spin-orbital-lock stripe configurations which differentiate by three choices of the principal lattice directions that stripes run along and two spin orientations within each stripe. For $J_1^{z\pm} = 0$, in the stripe-I phase, the spins lay in the xy plane and point perpendicular to the stripes [see FIG. 13 (a)], while in the stripe-II phase, the spins also lay in the xy plane but point along the principal axes $\pm a_1, \pm a_2, \mp a_1 \pm a_2$ [see FIG. 13 (b)]. The nonzero $J_1^{z\pm}$ will tilt the spins out of xy plane by an angle with the z axis.

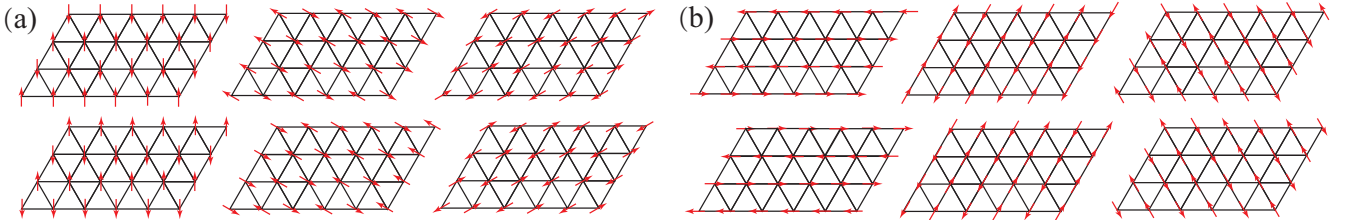


FIG. 13. Six basic magnetic structures for the (a) Stripe-I and (b) stripe-II phases when we take $J_1^{z\pm} = 0, J_2 = 0$.

To confirm the magnetic structures in the finite-size ED calculations, we plot the real-space spin correlations of all three components in the limits with only nonzero $J_1^{\pm\pm} = +1$ or $J_1^{\pm\pm} = -1$ or $J_1^{z\pm} = 1$ which are shown in FIG. 14, FIG. 15 and FIG. 16, respectively. We take the first lattice site as the reference site and show its spin correlations with all other sites. In the $J_1^{\pm\pm} = \pm 1$ case, the spin correlations of the six degenerate ground states in the finite-size ED calculations reflect the superpositions of the corresponding six basic magnetic structures, see FIG. 14 and FIG. 15.

Even though Stripe-I and Stripe-II phases are different phases, we still can use the square sublattice magnetization for the stripe orders (see the definition in the main text) to differentiate them with other phases. And the direction phase transition between two stripe phases will show a dip in the extrapolated results [see the inset of FIG. 3(b) in the main text].

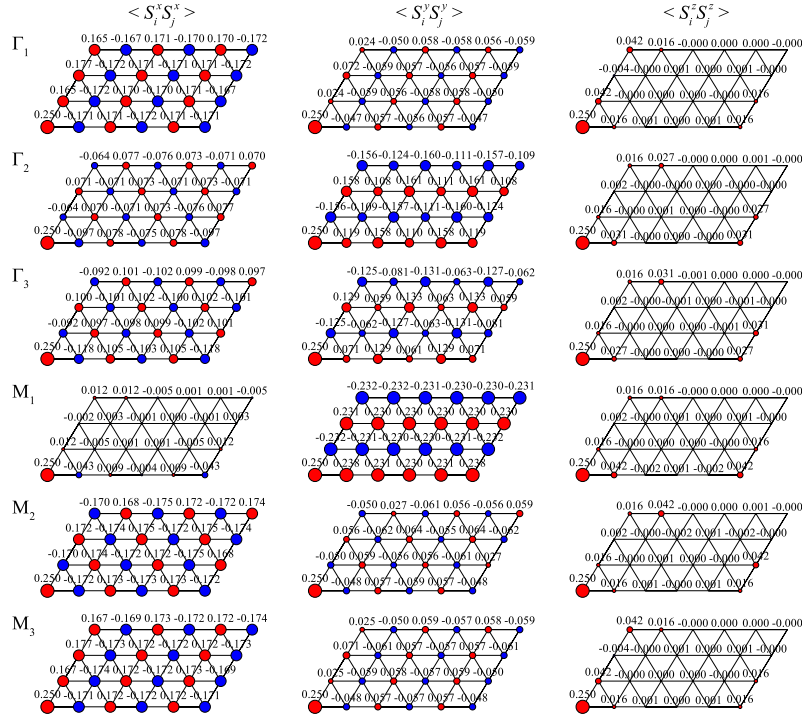


FIG. 14. Three components of the spin correlation functions at the $J_1^{\pm\pm} = +1$ limit with zero values of all other parameters. We use $24a$ cluster to do the calculations.

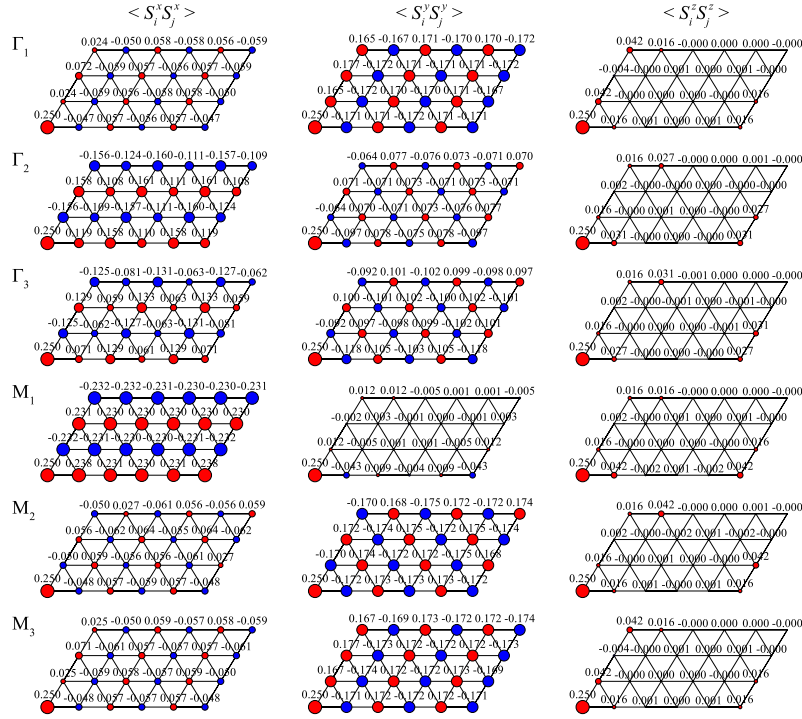


FIG. 15. Three components of the spin correlation functions at the $J_1^{\pm\pm} = -1$ limit with zero values of all other parameters. We use $24a$ cluster to do the calculations.

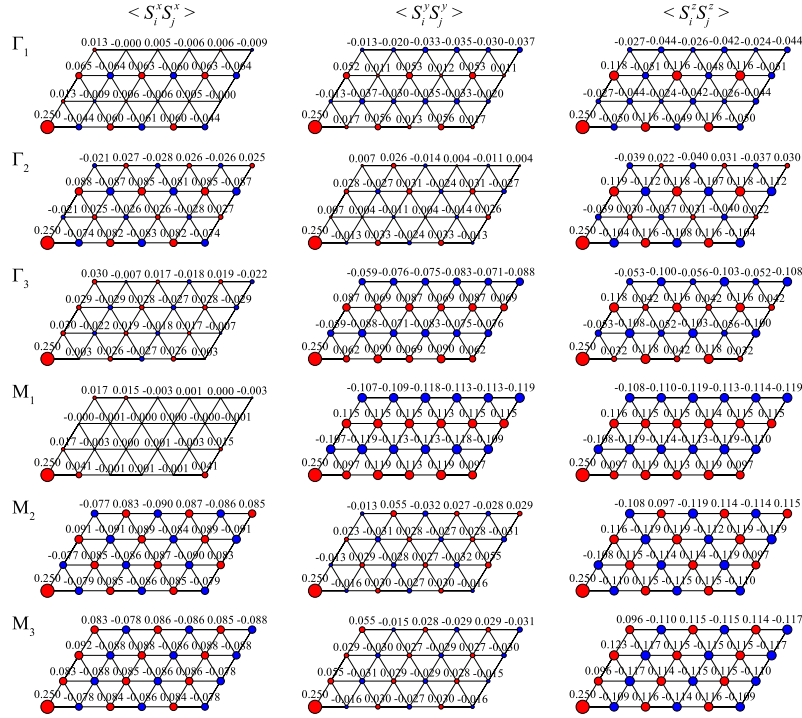


FIG. 16. Three components of the spin correlation functions at the $J_1^{z\pm} = 1$ limit with zero values of all other parameters. We use 24a cluster to do the calculations.

IV: FRUSTRATION PARAMETER

The frustration parameter is defined as $f = |\Theta_{CW}|/T_c$, where Θ_{CW} is the negative Curie-Weiss temperature and T_c is the critical temperature. We take the T_c approximately as the temperature T_m where the magnetic heat capacity gets its maximum value. Actually, $T_c \approx T_m$ works well in the stripe-I and stripe-II phases. However, in quantum spin liquid phase region, T_c is zero. In fact, the frustration parameter should be diverge. And the heat capacity still has a broad maximum at finite T . In the 120° Néel phase, the $J_1^{\pm\pm}$ and $J_1^{z\pm}$ interactions break the $U(1)$ continuous symmetry of the XXZ model. Especially, the $J_1^{\pm\pm}$ interaction would tilt the spins out of xy plane. Then whether the 120° Néel phase has a gap and a finite critical temperature are still unclear, which need further study in future. In any case, we can expect that T_c should be lower than the T_m . Therefore, the frustration parameter in the 120° Néel phase is underestimate. Even though, using $T_c \approx T_m$ may not correctly estimate the real frustration parameter. We still can use this approximation to compare the frustration of different phase regions in the 3D parameter space. As we have shown in the FIG.2 of the main text, the nonmagnetic quantum spin liquid region has a larger frustration parameter compared to other magnetic ordered phase regions, that is consistent with phase boundaries obtained by extrapolations of magnetic orders.

Here, we take the B set of parameters [see FIG. 2(a) in the main text] to representatively show the calculation of frustration parameter. The origin data of heat capacity and uniform magnetic susceptibility are shown in FIG. 17. These two observations are calculated by the following equations.

$$C_m = \frac{1}{Nk_B T^2} \left(\langle H^2 \rangle - \langle H \rangle^2 \right), \chi = \frac{1}{Nk_B T} \left(\langle M_z^2 \rangle - \langle M_z \rangle^2 \right)$$

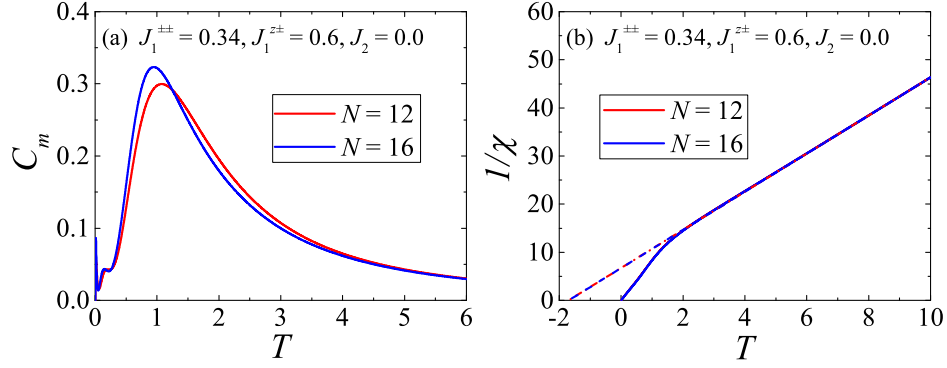


FIG. 17. (a) Magnetic heat capacity and (b) uniform magnetic susceptibility obtained by full exact diagonalization using 12 and 16 clusters. For 12 cluster, $T_m \approx 1.08$, $\Theta_{CW} \approx -1.70$, $f \approx 1.57$. For 16 cluster, $T_m \approx 0.95$, $\Theta_{CW} \approx -1.70$, $f \approx 1.79$. We take the Boltzmann constant $k_B = 1$ in drawing these two figures and use the B set of parameters to do the calculations. Two prominent peaks appear in the heat capacity. The first peak in the low temperature comes from the finite-size gap of ground-state manifold, this peak will shift to zero temperature when the system size goes to infinite. The second peak reflects the finite excitation gap above the GSM, this peak will diverge when the system size goes to infinite which indicates a spontaneously Z_6 symmetry breaking.

V: MAGNETIZATION CURVES

In this sector, we want to show more magnetization curves at different phases, including 120° Néel phase, Stripe-I phase and quantum spin liquid phase. In the main text, we have shown the magnetization curve of the QSL phase at $J_1^{\pm\pm} = -0.17$, $J_1^{z\pm} = 0.6$, $J_2 = 0.0$ under the external magnetic field applied perpendicular to the c axis, a clear $1/3$ -magnetization plateau has been observed. In FIG. 18, we show the magnetization curve of the same set of parameters under the external magnetic field applied parallel to the c axis. The $1/3$ -magnetization plateau seems still visible, but it may be quite narrow in the thermodynamic limit. The different results of two magnetic fields originate from the easy-plane anisotropic $\alpha > 1$ and the out of plane anisotropic $J_1^{z\pm}$.

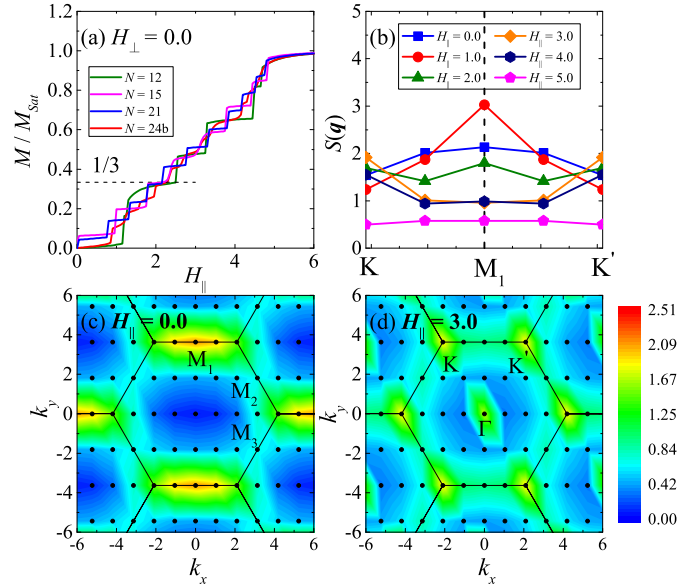


FIG. 18. (a) Magnetization curves of the QSL phase at $J_1^{\pm\pm} = -0.17$, $J_1^{z\pm} = 0.6$, $J_2 = 0.0$ under external magnetic field applied parallel to the c axis. (b) The spin structure factors $S(\mathbf{q})$ along $K \rightarrow M_1 \rightarrow K'$ high symmetry path in the Brillouin zone (BZ) under different strengths of magnetic field. (c) and (d) are the contour plots of spin structure factors in the whole BZ at $H_{\parallel} = 0$ and 3, respectively. We use the 24b cluster to get those results in (b), (c) and (d). The intensity of $S(K)$ at $H_{\parallel} = 3$ is weaker than the intensity of $S(M)$ at $H_{\parallel} = 0$.

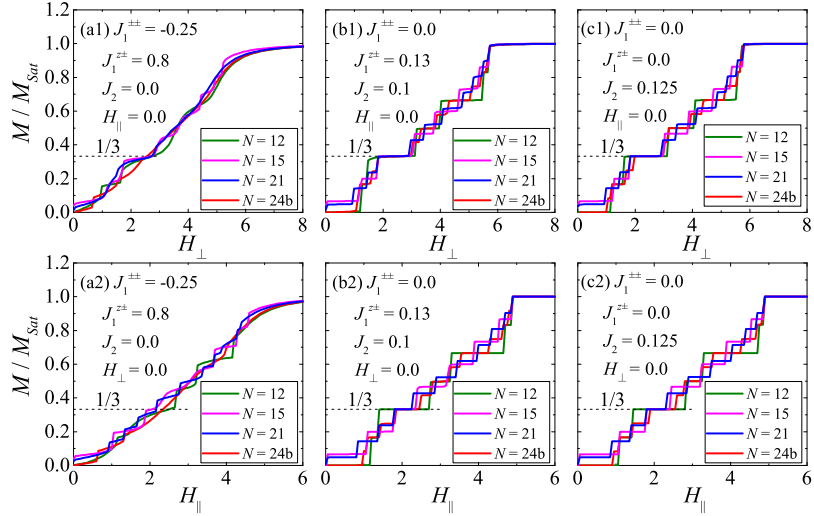


FIG. 19. Magnetization curves of the QSL phase at different sets of parameters under the external magnetic fields. (a1-c1) The magnetic fields are perpendicular to the c axis. (a2-c2) The magnetic fields are parallel to the c axis. The set of parameters used in (b1) and (b2) corresponds to C point of FIG. 2(c) in the main text.

The magnetization curves with other sets of parameters in the quantum spin liquid region are representatively shown in FIG. 19. In FIGS. 19 (a1) and 19(a2), because the out-of-plane interaction $J_1^{z\pm} = 0.8$ is large, it seems that the $1/3$ -magnetization plateau is already melted to be invisible, especially for the curve obtained by $24b$ cluster. And a more linear curve (in the thermodynamic limit) is observed when applying the field parallel to the c axis. For FIGS. 19 (b1) and 19(c1), the $J_1^{z\pm}$ interaction is small or zero, so we can reproduce flat $1/3$ -magnetization plateaux.

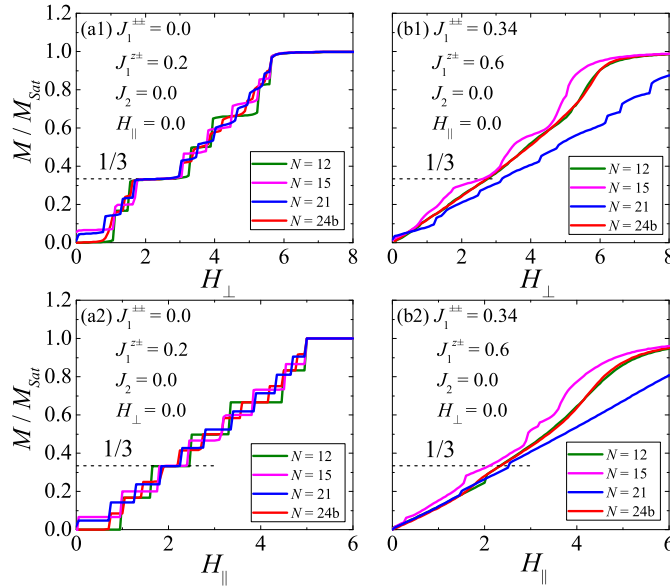


FIG. 20. Magnetization curves at different sets of parameters under external magnetic fields. (a1-b1) The magnetic fields are perpendicular to the c axis. (a2-b2) The magnetic fields are parallel to the c axis. (a1) and (a2) are for the 120° Néel phase. (b1) and (b2) are for the stripe-I phase.

We have also calculated the magnetization curves of 120° Néel phase and stripe-I phase in FIG. 20. In the 120° Néel phase, the $1/3$ -magnetization plateau is clearly seen. The nonflatness depends on the $J_1^{z\pm}$ interaction. In the stripe-I phase, there is no $1/3$ -magnetization plateau induced by two kinds of magnetic fields.

To show the effects of different parameters, like $J_1^{\pm\pm}$, $J_1^{z\pm}$, J_2 , on the $1/3$ -magnetization plateau, we use $24b$ cluster to show the change of magnetic curves with these parameters, which are shown in FIG. 21. When $J_1^{\pm\pm}$, $J_1^{z\pm}$, J_2 are

small and the system is in 120° Néel phase, the $1/3$ -magnetization plateau is flat. In the quantum spin liquid phase region with large $J_1^{z\pm} > 0.5$, the $1/3$ -magnetization plateau is melted to nonlinear rough curve, see FIG. 21(a1). When we increase $J_1^{\pm\pm}$ and keep $J_1^{z\pm} = 0$, the flatness of plateau is nearly unchanged. After $J_1^{\pm\pm} > 0.2$ which drives system into Stripe-I phase, the plateau quickly melts to a linear curve, see FIG. 21(b1). For the $J_1 - J_2$ XXZ model, in the 120° Néel and the QSL phase regions, the $1/3$ -magnetization plateau is flat and has nonzero width ΔH_\perp in the thermodynamic limit [see the inset of FIG. 21(c1)]. When $J_2 > 0.175$, the system is in the stripe phase with three-fold ground state degeneracy, the $1/3$ -magnetization plateau disappears [see the inset of FIG. 21(c1)]. Instead, a $1/2$ -magnetization plateau appears.

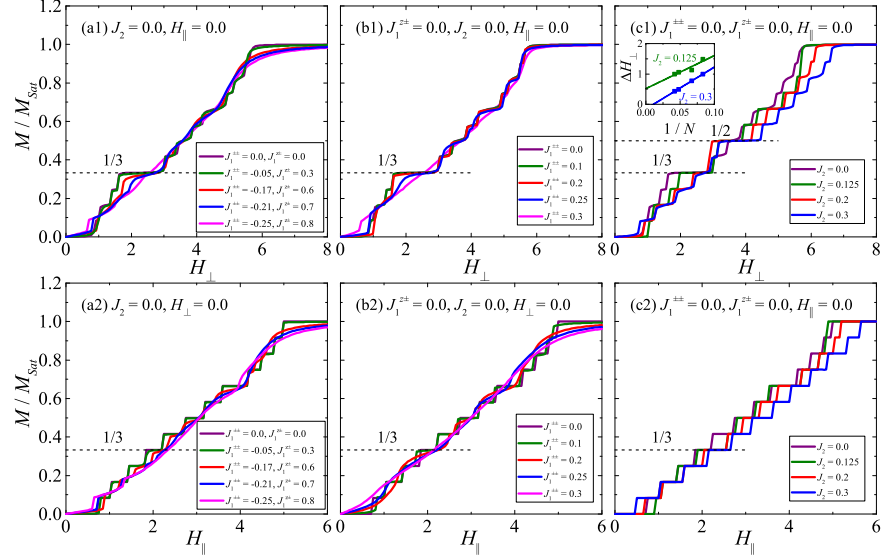


FIG. 21. Finite-size magnetization curves obtained by $24b$ cluster along different paths in the 3D parameter space. (a1-c1) The magnetic fields are perpendicular to the c axis. (a2-c2) The magnetic fields are parallel to the c axis. The inset of (c1) shows linear extrapolations of the $1/3$ -plateau-width as functions of $1/N$.

To verify the $1/3$ -magnetization plateau phase is a “uud” phase. We have calculated the energy spectrum and the spin correlation functions at $J_1^{z\pm} = -0.17$, $J_1^{\pm\pm} = 0.6$, $J_2 = 0.0$, $H_\perp = 1.8\sqrt{2}$, $H_\parallel = 0$, see FIG. 22. From the low energy spectrum, we find three-fold quasi-degenerate ground states. Through finite-size scalings, we can observe the exact degeneracy (before spontaneously Z_3 symmetry breaking) and a finite energy gap above the ground states. And we show the real-space spin correlation functions of these three ground states in FIG. 23, the “uud” structure can be clearly seen.

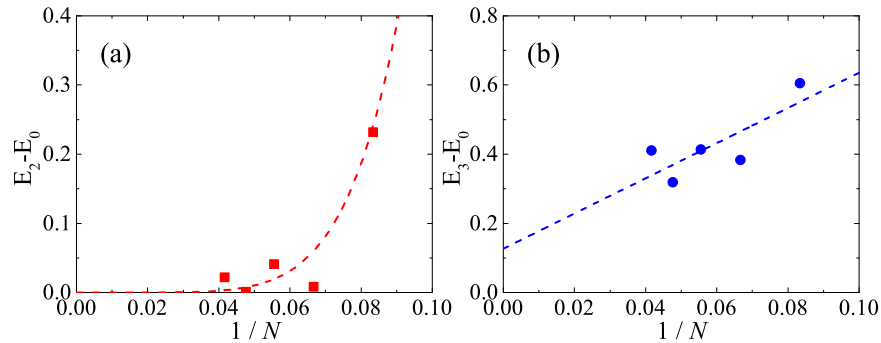


FIG. 22. (a) The finite-size gap of the ground state manifold as a function of $1/N$. The red dashed line is a guide to the eye. This gap would be zero when $N \rightarrow \infty$. (b) Linear extrapolation of the excitation gap above ground state manifold. The finite extrapolated value indicates a finite excitation gap. We take $J_1^{z\pm} = -0.17$, $J_1^{\pm\pm} = 0.6$, $J_2 = 0.0$, $H_\perp = 1.8\sqrt{2}$, $H_\parallel = 0$ which corresponds to $1/3$ -magnetization plateau phase or “uud” phase region in the ED calculation [see FIG. 6(a) in the main text].

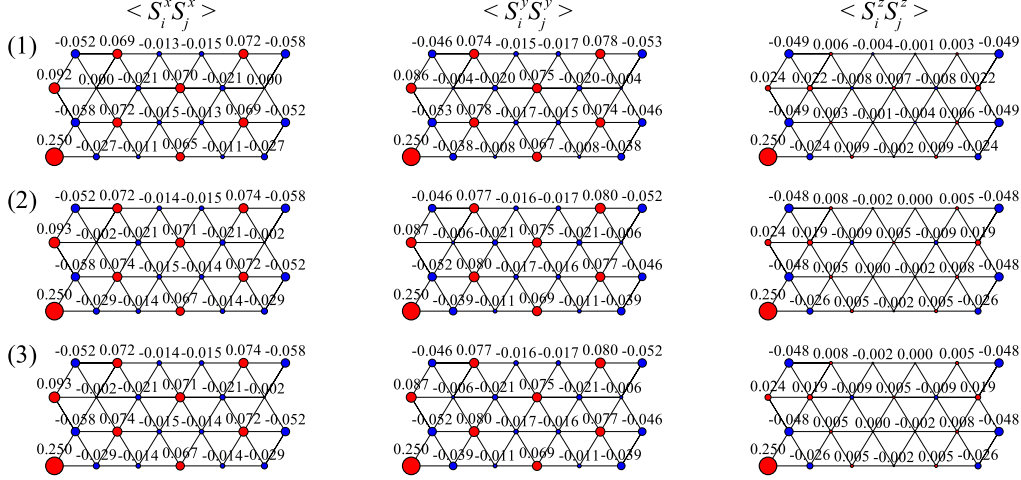


FIG. 23. Three components of the spin correlation functions at $J_1^{\pm\pm} = -0.17$, $J_1^{z\pm} = 0.6$, $J_2 = 0.0$, $H_{\perp} = 1.8\sqrt{2}$, $H_{\parallel} = 0$ [see FIG. 6(a) in the main text]. Two antiferromagnetic nearest-neighbor (n.n.) correlation bonds and one ferromagnetic n.n. correlation bond are found within one triangle.

VI: BOND RANDOMNESS EFFECTS

We have introduced bond randomness into the Hamiltonian to simulate the chemical disorders. For the 120° Néel phase, the strongest randomness at $\Delta = 1$ can eliminate this magnetic order, which can be seen FIG. 24 (a). For the stripe phases, the magnetic orders are stable against the bond randomness. The stripe orders cannot be eliminated even in the strongest bond randomness case, as can be seen FIG. 24 (b).

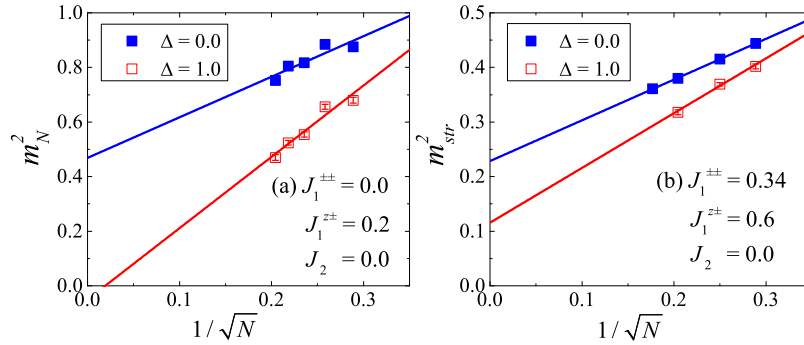


FIG. 24. Linear extrapolations of the square sublattice magnetizations for (a) the 120° Néel phase at $J_1^{\pm\pm} = 0.0$, $J_1^{z\pm} = 0.2$, $J_2 = 0.0$. and (b) the Stripe-I phase at $J_1^{\pm\pm} = 0.34$, $J_1^{z\pm} = 0.6$, $J_2 = 0.0$.

The above discussions focus on ground state properties at zero temperature. Here, we want to discuss the bond randomness effects on stripe-I phase at finite temperature. We take the B set of parameters [see FIG. 2(a) in the main text] to show the measurements. In the strongest-randomness limit, there is only one broad peak in the magnetic heat capacity C_m . Most interestingly, a power-law behavior $C_m \sim T^\delta$ is observed in the low temperature regime, as can be seen in FIG. 25. δ obtained by fitting the C_m curve from $T = 0.1$ K to $T = 0.25$ K using 16 cluster is approximately 0.69 which is very close to $2/3$. And the heat capacity obtained by 12 and 16 clusters under the strongest bond randomness are qualitatively (even quantitatively) the same as the experimental one of YbMgGaO_4 [7, 12]. So surprisingly, a spin-liquid-like behavior has been observed in the strongest bond-randomness limit of the Stripe-I phase.

In the strong randomness case, the finite-size effect is actually not severe. So the 12 cluster is able to capture the main physics in the strongest bond-randomness limit. In this limit, the heat capacity has a broad peak, and

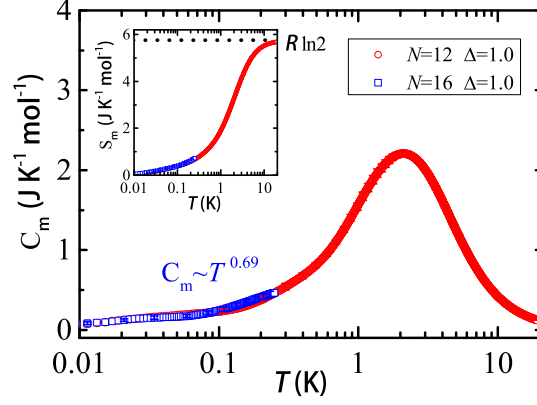


FIG. 25. The magnetic heat capacities C_m obtained by 12 and 16 clusters in the strongest bond randomness limit $\Delta = 1$. Here, we use the B set of parameters: i.e. $J_1^{\pm\pm}/J_1 = 0.34$, $J_1^{z\pm}/J_1 = 0.6$, $J_2/J_1 = 0$, and use $J_1 = 0.164$ meV [24] to do the ED calculations. For the 16 cluster, we employ Lanczos method to calculate the heat capacity at low temperature. The restriction of Boltzmann factor $e^{-(E_{max}-E_0)/k_B T} < 10^{-12}$ has been used to determine the upper-bound temperature below which the calculated C_m is trustable. And we have used at least 20 bond-randomness samples to get the averaged $C_m(T)$. The inset shows the magnetic entropy $S_m = \int_0^T C_m/T dT$. No residual entropy is found in low temperature.

this peak will not diverge with the increasing system size. That means even though the ground state of the system has residual stripe order, but it may be hard to probe this order at finite temperature. Actually, previous classical Monte Carlo simulation from Ref. 20 has shown the similar behavior in the heat capacity. In the clean case, there is a single continuous transition with slowly diverging heat capacity. In the randomness case, this transition is removed by fragmenting the system into domains.

We have also calculated the heat capacity with other set of parameters (especially for the QSL phase region) under strongest bond randomness. However, none of those can reproduce nearly the same heat capacity as the experimental one, which are show in FIG. 26. In the clean limit, whether we can get the same heat capacity as the experimental one using some sets of paramters is still an open question. Recently, a finite-temperature Lanczos methods with improved accuracy [K. Morita and T.Tohyama, Phys. Rev. Res. 2, 013205 (2020)] has successfully applied to Kitaev-Heisenberg model on Kagome and triangular lattices, which would be a great help to study the finite-temperature properties of the model related to YbMgGaO₄ in future.

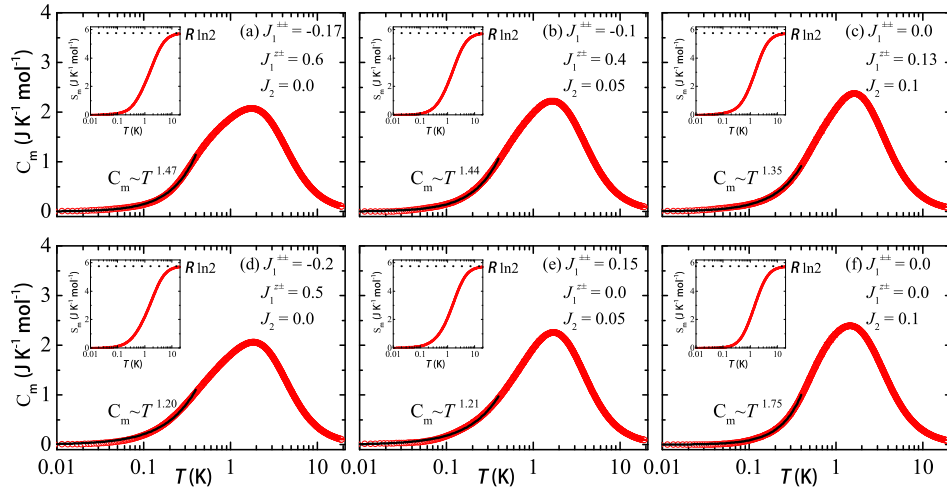


FIG. 26. The magnetic heat capacities C_m obtained by 12 cluster in the strongest bond randomness limit $\Delta = 1$. Here, we use $J_1 = 0.164$ meV to show all the data. And we have used at least 50 bond-randomness samples to get the averaged $C_m(T)$. The insets show the magnetic entropy $S_m = \int_0^T C_m/T dT$.

VII: XXZ ANISOTROPIC EFFECTS

To see how the XXZ (or easy-plane) anisotropic α affects the phase diagram, we use fidelity susceptibility of $24a$ cluster to get the 120° Néel phase boundaries under different α , and use the linear extrapolations of the stripe orders mainly with 16 and $24a$ clusters to get the phase boundaries of stripe phases. Then we obtain some phase diagrams under different α which are shown in FIG. 27. When α decreases, the (deformed) 120° Néel phase and the QSL phase regions shrink. Especially for the QSL phase, at $\alpha = 0.5$, this phase region is too small to identify. In the limit of $\alpha = 0$, the 120° Néel phase region will quickly vanish (see FIG. 28). When α is large, both of the 120° Néel phase and the QSL phase seem to extend to larger areas. Please remind that we have taken $J_1 = 1$ (actually $J_1^{zz} = 1$) as energy constant. If we take $J_1^\pm = 1$ as the new energy constant, the volume of QSL phase may decrease to a finite constant when we increase α from 1 to larger values. In the limit $\alpha = \infty$ or $J_1^{zz} = J_2^{zz} = 0$, unlike the $\alpha = 0$ limit, the quantum spin liquid phase will survive [see N. Suzuki et al., Journal of Modern Physics, 10, 8-19 (2019)]. Compared with previous DMRG study from Ref. 18 and Ref. 19, our QSL regions are more naturally located between three magnetic ordered phases due to the order-by-disorder effect and extend to the $J_1^{\pm\pm}$ axis in the $J_2 - J_1^{\pm\pm}, J_1^{zz} = 0$ plane. More importantly, the critical $\alpha_c \sim 0.5$ where the QSL disappears is obtained from our ED calculations.

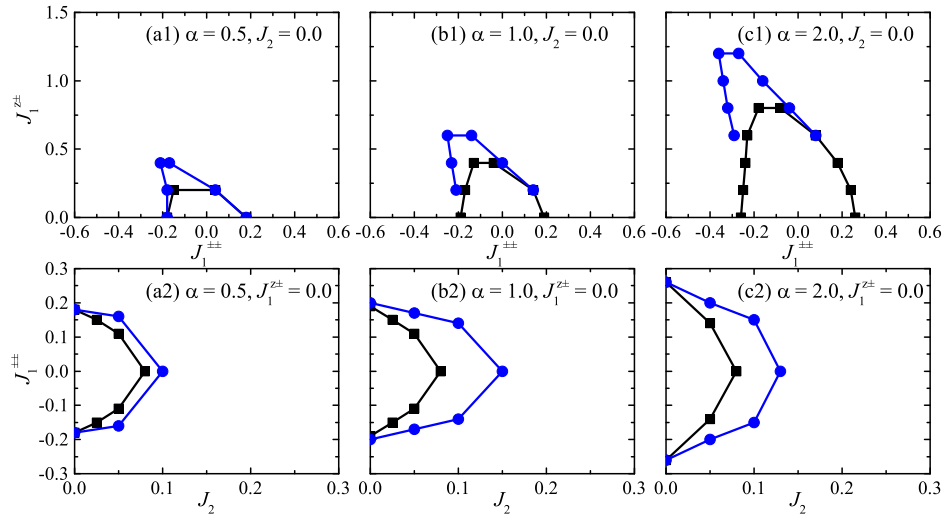


FIG. 27. The phase diagrams with different easy-plane anisotropic α . (a1-c1) is the phase diagrams on the $J_2 = 0, J_1^{\pm\pm} - J_1^{zz}$ plane. (a2-c2) is the phase diagrams on the $J_1^{zz} = 0, J_2 - J_1^{\pm\pm}$ plane. We only show the 120° Néel phase and the QSL phase regions here.

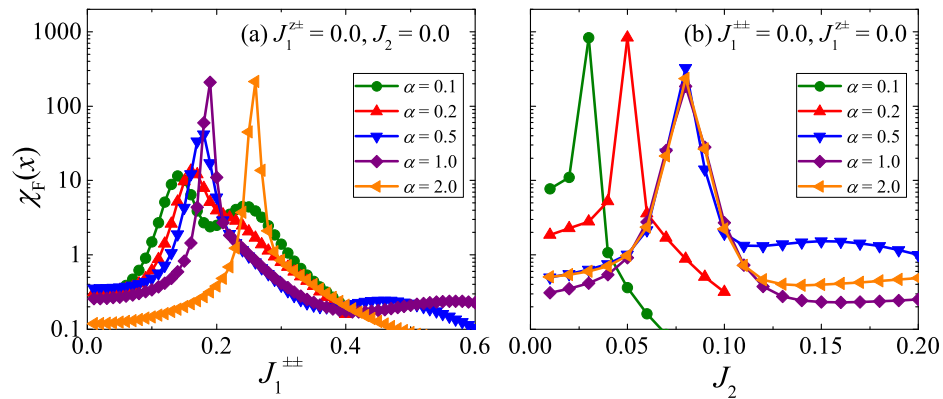


FIG. 28. (a) The fidelity susceptibilities as functions of $J_1^{\pm\pm}$ under different XXZ anisotropic α and along the $J_1^{\pm\pm}$ axis. (b) The fidelity susceptibilities as functions of J_2 under different XXZ anisotropic α and along the J_2 axis. When $\alpha < 0.5$, the phase transition point $J_{2,c}$ starts to drop quickly.

VIII: DYNAMICAL SPIN STRUCTURE FACTOR

We have calculated the dynamical spin structure factor in the QSL region which can be computed by continued fraction expansion,

$$\begin{aligned}
 S^{\alpha\alpha}(\mathbf{q}, \omega) &= \sum_n \left[|\langle \psi_n | \hat{S}_{\mathbf{q}}^{\alpha} | \psi_0 \rangle|^2 \delta(\omega - (E_n - E_0)) \right], \\
 &= -\frac{1}{\pi} \lim_{\eta \rightarrow 0} \text{Im} \left[\langle \psi_0 | \left(\hat{S}_{\mathbf{q}}^{\alpha} \right)^{\dagger} \frac{1}{\omega + E_0 - \hat{H} + i\eta} \hat{S}_{\mathbf{q}}^{\alpha} | \psi_0 \rangle \right], \\
 &= -\frac{1}{\pi} \lim_{\eta \rightarrow 0} \text{Im} \left[\frac{\langle \psi_0 | \left(\hat{S}_{\mathbf{q}}^{\alpha} \right)^{\dagger} \hat{S}_{\mathbf{q}}^{\alpha} | \psi_0 \rangle}{\omega + E_0 + i\eta - a_0 - \frac{b_1^2}{\omega + E_0 + i\eta - a_1 - \frac{b_2^2}{\omega + E_0 + i\eta - a_2 \dots}}} \right], \alpha = x, y, z.
 \end{aligned}$$

where a_i and b_{i+1} are the diagonal and subdiagonal elements of the tridiagonal Hamiltonian matrix obtained by the Lanczos method with initial vector $\hat{S}_{\mathbf{q}}^{\alpha} | \psi_0 \rangle$. In experiment, the dynamical spin structure factor can be studied by inelastic neutron scattering (INS) or X-ray Raman scattering. Here, we show the ED results using $24b$ cluster in FIG. 29. At $J_1^{\pm\pm} = -0.17$, $J_1^{z\pm} = 0.6$, $J_2 = 0.0$, though there are finite-size effects, we still can observe that the low-energy maxima are located at M points. And the maxima at K points are at higher energy. It seems that our ED calculations are consistent with the inelastic neutron scattering measurements of YbMgGaO_4 [6, 7]. While using the C set of parameters, the maxima in K and M points are nearly at the same energy. It can be easy to understand this phenomenon. Starting from 120° Néel phase to the QSL phase, and then to a stripe phase, the spectral weight would transfer from K points to the M points. In the intermediate QSL region, it is possible that the low-energy maxima locate at either K points or M points.

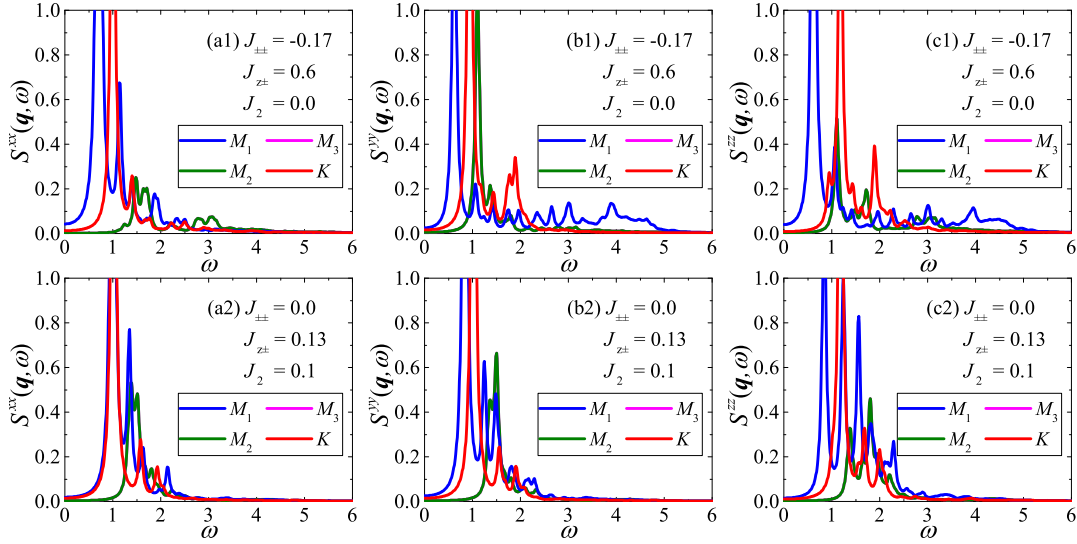


FIG. 29. The dynamical spin structure factors of the QSL phase at two K points and three M points using different sets of parameters. The XXZ anisotropic α is set to be 1.317. Three M points are not equivalent in $24b$ cluster. The parameters we choose for (a1-c1) are $J_1^{\pm\pm} = -0.17$, $J_1^{z\pm} = 0.6$, $J_2 = 0.0$. And (a2-c2) use the C set of parameters which is shown in FIG. 2(c) in the main text. The Lorentz broadening factor we use is $\eta=0.05$.

IX: SOME DISCUSSIONS ABOUT NaYbCh_2

Both YbMgGaO_4 and NaYbCh_2 (Ch=O,S,Se) share the same space symmetry group $R\bar{3}m$ and the perfect triangular magnetic layers which consist of Yb^{3+} ions. Recent experiments [9, 39–44] have revealed that the interlayer Yb-Yb

distance in NaYbO_2 and NaYbS_2 is shorter than YbMgGaO_4 . Most importantly, the interlayer Yb-Yb distance is nearly equivalent with the next-nearest-neighbor in-plane distance, which means the interlayer interactions are relevant in the low temperature exchange model. A more complicated exchange Hamiltonian with the same in-plane part as the YbMgGaO_4 and compass-like interlayer exchange interactions has been proposed to understand macroscopic behaviors of these materials [see Ref. 44 for more details]. However, if we can neglect the chemical disorders, the single-layer model for YbMgGaO_4 may still can describe the quantum spin liquid behavior of NaYbCh_2 if the interlayer interactions are some small effects. What's more, it seems that the $1/3$ -magnetization plateau is more clearly seen in the magnetization curve of NaYbCh_2 . In addition, we still need cautions about the possible randomness effects on NaYbCh_2 , such as Na sites occupied by the Yb ions in NaYbSe_2 [11]. All of these issues, including the interlayer interactions and magnetic impurities between Yb layers, need further investigations beyond the classical Heisenberg model analysis in future [44].